Inverse identification of large strain plasticity using the hydraulic bulge-test and full-field measurements

Marco Rossi [a,*], Attilio Lattanzi [a], Frédéric Barlat [b], Jin-Hwan Kim [b]

[a] *Faculty of Engineering, Università Politecnica delle Marche, 60131 Ancona, Italy*
[b] *Graduate Institute of Ferrous and Energy Materials Technology (GIFT), Pohang University of Science and Technology (POSTECH), 77 Cheongam-ro, Nam-gu, Pohang, Gyeongbuk 37673, Republic of Korea*

ARTICLE INFO

ABSTRACT

The hydraulic bulge test (HBT) is an important experimental technique to identify the properties of materials and, in particular, metals. One of the main advantages of such technique, in testing metals, is the possibility of reaching high levels of deformation before fracture. Moreover it allows the investigation of a biaxial loading condition. A hemispherical test can be performed using mechanical punches or the hydraulic pressure of a fluid. When hydraulic pressure is used, the test is not affected by friction. The hydraulic bulge test (HBT) is therefore a very efficient method to evaluate the properties of metals at large strains. Usually, the outcome of the HBT is the hardening curve in the equi-biaxial stress state that occurs at the top of the dome, during the expansion. In this paper a different approach is proposed, where the full-field displacement field obtained with stereo-DIC is used in an inverse identification scheme. The finite strain theory is used to map the stress and strain in the reference configuration so that the problem can be reduced to a 2D plane stress case. The method was first validated using a numerical model of the HBT and then applied on a real test performed on a BH340 steel.

1. Introduction

The hydraulic bulge test (HBT) represents an effective and well established experimental procedure to identify the properties of materials (Bunge et al., 2000). The test is performed placing a blank sheet under a die with a circular aperture, the sheet is clamped at the borders and deformed by the action of a fluid applied to one side. When the bulge is formed, the stress state in proximity of the dome apex can be approximated to the membrane stress of a thin-walled spherical vessel, enabling the calculation of the true stress–true strain curve from the local curvature. With respect to the standard uniaxial tensile tests, the HBT allows to achieve a much larger deformation, because the plastic instability and the localized necking is postponed. Many examples can be found in the literature where the HBT is used to characterize the large strain behavior of ductile metals, for instance, applications were presented by Gutscher et al. (2004) and Chen et al. (2018). Moreover, during the HBT, the material is deformed according to a nearly equi-biaxial state of stress, therefore it is an important experimental method to identify the material behavior in multiaxial loading conditions; for instance, Barlat et al. (2005) and Chen et al. (2016) used the bulge test to calibrate the yield function of advanced anisotropic models. In practice, the HBT is often used in combination with other tests (e.g. tensile tests, shear tests, etc.) to improve the material characterization (Zang et al., 2011; Pradeau et al., 2016; Hérault et al., 2021). The HBT was applied to many different problems related to material testing, for instance, Barnwal et al. (2021) used it to study fracture in metals and Lee et al. (2013) to evaluate the performance of materials in warm conditions by heating the fluid under pressure. Modified versions of the HBT, which exploit a similar working principle, were also proposed by Kuwabara and Sugawara (2013), for instance, in order to analyze mixed loading conditions, the hydraulic pressure was combined with axial tension through a multiaxial tube expansion test. Another variation, proposed by Williams and Boyle (2016), consists in performing a HBT with an elliptical hole to study the anisotropic behavior of metals.

From an experimental point of view, one of the key points of the HBT is the determination of the radii of curvature in the dome, which is used to compute the true stress. In the past, the calculation was based on the measurement of the peak height during the tests, as illustrated in the pioneering work of Hill (1950), or using a spherometer (Young et al., 1981). Nowadays, optical systems and full-field measurements are usually preferred because of their accuracy as demonstrated by Koç et al. (2011). The ISO 16808:2014 standard specifies a procedure to

obtain the biaxial stress–strain curve using optical measurement systems, however, Mulder et al. (2015) proposed an alternative method to increase the accuracy and the problem of stress–strain measurement in the bulge test is still a research topic. Recently, Chen (2020) presented a general theory to extract the stress and strain curve at the apex of a bulge test that holds for both circular and elliptical bulge test, irrespective of material properties.

In this paper a different approach is proposed, the displacement field measured during the bulge test through digital image correlation (DIC) (Sutton et al., 2009) is exploited to identify the materials properties applying an inverse identification scheme (Grédiac and Hild, 2013). Inverse methods are well documented in many applications of material characterization, see for instance the review of Avril et al. (2008), however, they are still not used for the HBT, where the standard procedures described above are primarily adopted. Inverse methods have some advantages with respect to the standard methods, in particular they allow to extract more information from a single test using the heterogeneous strain fields measured during the test in the specimen surface. Several inverse strategies can be used to identify the material properties from full-field measurement, among the most used, we can name the finite element model updating (FEMU) and the virtual fields method (VFM). According to FEMU, a virtual copy of the test is reproduced with finite elements and the constitutive parameters are iteratively changed in order to obtain the best match between experiments and numerical results. Many examples can be found in plasticity (Meuwissen et al., 1998; Cooreman et al., 2008; Prates et al., 2016), including identification at large strains (Kajberg and Lindkvist, 2004), and application to complex anisotropic models (Kajberg and Lindkvist, 2004). The VFM, instead, uses directly the strain full-field data measured during the experiment to write the static equilibrium law as a function of the constitutive parameters, employing the principle of virtual work (Pierron and Grédiac, 2012). In case of non-linear models, the constitutive parameters can be then identified using a minimization algorithm. The VFM was applied successfully in plasticity, Rossi and Pierron (2012) developed an algorithm for large deformation, Rossi et al. (2016), Kim et al. (2014), Fu et al. (2017) and Lattanzi et al. (2020) studied in details the possibility of applying the VFM for anisotropic plasticity. With respect to FEMU, the VFM does not require the use of FE models, thus is usually computationally more efficient, as shown by Zhang et al. (2017), and is less affected by the boundary conditions. On the other hand, VFM is sometimes less flexible than FEMU, because it requires the strain measurement over the whole surface area of the specimen and an assumption about the through thickness deformation, e.g. plane stress or plane strain hypothesis. Other inverse methods, similar to VFM, were proposed to use directly the full-field data to identify, for instance the post-necking behavior of metals (Coppieters et al., 2011; Rossi et al., 2018b).

Most of the cited inverse methods were developed for 2D problems, since full 3D measurements are still difficult to obtain, especially for metals, although some attempts of using interpolation functions to investigate the internal deformation of solids where recently developed by Rossi et al. (2018a). In the HBT, the plane stress hypothesis is acceptable, however the deformation is three dimensional. In this paper, finite deformation theory is used to provide a framework that enables to efficiently implement the HBT in inverse methods, using the full-field data measured from stereo-DIC. The method is described in Section 2, a numerical validation is given in Section 3 and a demonstration on a real experiment is presented and discussed in Sections 4 and 5.

2. Method description

During the HBT, a blank sheet is deformed by the hydraulic pressure of a fluid. Let us consider a Cartesian coordinate system with the origin placed at the center of the initial blank sheet and the z-axis oriented perpendicular to the sheet surface. In the undeformed or reference configuration $\mathscr{B}_0$, the position of each point P of the sheet can be

identified by a set of coordinates $\mathbf{X}$, in the X–Y plane so that $\mathbf{X} = [X, Y, 0]$. At the time step t of the test, the new position of point P in the deformed configuration $\mathscr{B}$ will be $\mathbf{x} = [x, y, z]$, as illustrated in Fig. 1.

At a given time t, for each point P we can associate a thickness $s(P, t)$ and a surface normal $\hat{\mathbf{n}}(P, t)$. It is worth noting that in the reference configuration $\mathscr{B}_0$, the thickness s_0 is constant and the surface normal is always equal to $\hat{\mathbf{n}}_0 = [0, 0, 1]$, according to the chosen coordinate system.

Applying the finite strain theory, the deformation is described by the deformation gradient $\mathbf{F}$, defined as:

$$\mathbf{F} = Grad\ \chi(\mathbf{X}, t) \tag{1}$$

with χ a function that, at each time step t, transforms the coordinates of a point P from the reference to the deformed configuration, i.e. $\mathbf{x} = \chi(\mathbf{X}, t)$. Expressing the component of $\mathbf{F}$ in a matrix format, it follows[1]:

$$\mathbf{F} = \begin{bmatrix} \frac{\partial x}{\partial X} & \frac{\partial x}{\partial Y} & \frac{\partial x}{\partial Z} \\ \frac{\partial y}{\partial X} & \frac{\partial y}{\partial Y} & \frac{\partial y}{\partial Z} \\ \frac{\partial z}{\partial X} & \frac{\partial z}{\partial Y} & \frac{\partial z}{\partial Z} \end{bmatrix} \tag{2}$$

The first two columns of $\mathbf{F}$ can be readily determined from the surface data, however the third column is undetermined since there is no information about the through-thickness behavior of the sheet. Using the polar decomposition, the deformation gradient $\mathbf{F}$ can be divided in the rotation matrix $\mathbf{R}$ and the right stretch tensor $\mathbf{U}$:

$$\mathbf{F} = \mathbf{R} \cdot \mathbf{U} \tag{3}$$

where $(\cdot)$ is a matrix multiplication. The right stretch tensor $\mathbf{U}$ is a symmetric tensor that maps the deformation in the undeformed configuration and can be computed directly from the deformation gradient as:

$$\mathbf{U} = \sqrt{\mathbf{F}^T \cdot \mathbf{F}} \tag{4}$$

making the assumption that there are not shear strains through the thickness, the components of $\mathbf{U}$ corresponding to the shear in the Z-direction can be set to zero:

$$\mathbf{U} = \begin{bmatrix} U_{11} & U_{12} & 0 \\ U_{21} & U_{22} & 0 \\ 0 & 0 & U_{33} \end{bmatrix} \tag{5}$$

then, if the $\mathbf{U}$ of Eq. (5) is input in the matrix multiplication of Eq. (3), it turns out that the third column of $\mathbf{F}$ is equal to:

$$\begin{bmatrix} \frac{\partial x}{\partial Z} \\ \frac{\partial y}{\partial Z} \\ \frac{\partial z}{\partial Z} \end{bmatrix} = U_{33} \begin{bmatrix} R_{13} \\ R_{23} \\ R_{33} \end{bmatrix} \tag{6}$$

where R_{ij} are the components of the rotation matrix $\mathbf{R}$. By definition of the rotation matrix, each column of $\mathbf{R}$ can be interpreted as a unit vector that represents the rotated orthonormal basis. In this sense, according to the chosen coordinate system, the third column of $\mathbf{R}$ in Eq. (6) is exactly the surface normal $\hat{\mathbf{n}}$, that represents the rotation of the basis vector corresponding to Z-direction, i.e. $\hat{\mathbf{n}}_0 = [0, 0, 1]$. For each point P, the normal $\hat{\mathbf{n}}$ can be easily computed from the surface data, using suitable normal detection algorithms. Making the further hypothesis of volume constancy, which is usually valid in large strain plasticity, it follows that $\det(\mathbf{U}) = 1$ and U_{33} can be derived, exploiting the properties of the determinant, as:

$$\det \mathbf{U} = U_{33} \cdot \det \mathbf{U}_1 \quad \text{with} \quad \mathbf{U}_1 = \begin{bmatrix} U_{11} & U_{12} \\ U_{21} & U_{22} \end{bmatrix} \tag{7}$$

---

[1] For the sake of simplicity, since an orthogonal Cartesian system is used, tensors are here represented directly as matrices, although formally this is not exact since matrices and tensors are different entities, and the matrix representation of the tensor components depends on the used basis vectors.
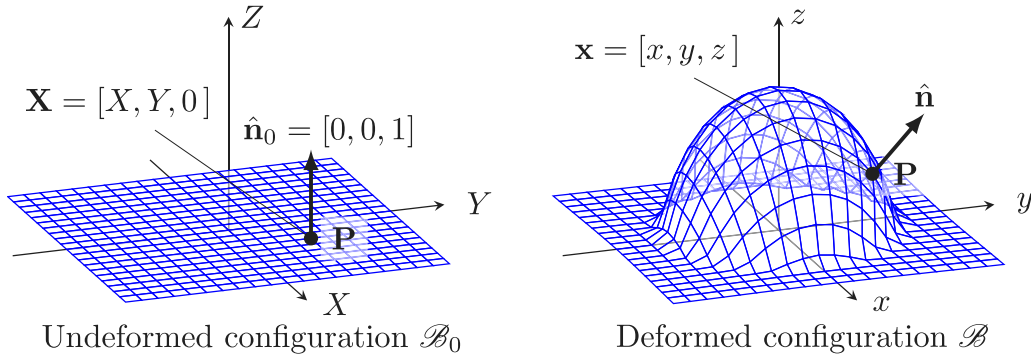
Fig. 1. Schematic of the initial and deformed sheet, the used coordinate system and the pressure distribution are illustrated.

using Eq. (8), it can be shown that the sub-matrix $\mathbf{U}_1$ only depends on the first two columns of $\mathbf{F}$, that is:

$$\mathbf{U}_1 = \sqrt{\mathbf{F}_1{}^T \cdot \mathbf{F}_1} \quad \text{with} \quad \mathbf{F}_1 = \begin{bmatrix} \frac{\partial x}{\partial X} & \frac{\partial x}{\partial Y} \\ \frac{\partial y}{\partial X} & \frac{\partial y}{\partial Y} \\ \frac{\partial z}{\partial X} & \frac{\partial z}{\partial Y} \end{bmatrix} \tag{8}$$

where $\mathbf{F}_1$ can be computed from the surface data since only derivatives along X and Y are involved. Eq. (6) can be rewritten as:

$$\begin{bmatrix} \frac{\partial x}{\partial Z} \\ \frac{\partial y}{\partial Z} \\ \frac{\partial z}{\partial Z} \end{bmatrix} = \frac{1}{\det(\mathbf{U}_1)} \begin{bmatrix} \hat{n}_x \\ \hat{n}_y \\ \hat{n}_z \end{bmatrix} \tag{9}$$

Finally, the complete rotation matrix can be obtained from the polar decomposition as:

$$\mathbf{R} = \mathbf{F} \cdot \mathbf{U}^{-1} \tag{10}$$

For each point $\mathbf{P}$ at the time step t, the matrices $\mathbf{F}$, $\mathbf{R}$ and $\mathbf{U}$ completely define the deformation state. Since the deformed configuration of the sheet metal during the test can assume a rather complex shape, it is useful to map strain and stress back in the reference configuration $\mathscr{B}_0$. To this purpose, the strain is computed as the material logarithmic strain tensor $\mathbf{E}$:

$$\mathbf{E} = \log(\mathbf{U}) \tag{11}$$

and the first Piola–Kirchhoff stress $\mathbf{T}^{1PK}$ is used instead of the Cauchy stress $\mathbf{T}$. The Cauchy stress $\boldsymbol{\sigma}$ represents the actual stress state, mapped in the current deformed configuration $\mathscr{B}$, the first Piola–Kirchhoff stress $\mathbf{T}^{1PK}$, instead, applies the external forces to the undeformed configuration $\mathscr{B}_0$, similarly to what the engineering stress does in one dimension. It can be computed from $\boldsymbol{\sigma}$ as:

$$\mathbf{T}^{1PK} = \det(\mathbf{F}) \, \boldsymbol{\sigma} \, \mathbf{F}^{-T} \tag{12}$$

The advantages of this approach in data processing will be evident later in the paper.

2.1. Stress–strain curve derivation

Let us consider a circular portion of the blank sheet $\mathscr{A}$ with a radius R_0 in the undeformed configuration as illustrated in Fig. 2. The stress in R_0 can be derived using the equilibrium between the load applied by pressure in $\mathscr{A}$ and traction force $\mathbf{dt}$ of the material at the boundary $\partial \mathscr{A}$, similarly to the classical Barlow's formula for tubes and vessels.

The resultant force due to the pressure is indicated with $\mathbf{f}^{(p)}$ and given by:

$$\mathbf{f}^{(p)} = \int_{\mathscr{A}} p \, \hat{\mathbf{n}} \, dA \tag{13}$$

where p is the pressure magnitude, dA the infinitesimal area and $\hat{\mathbf{n}}$ the normal unit vector. The pressure force can be computed in terms of the undeformed configuration $\mathscr{A}_0$ as:

$$\mathbf{f}^{(p)} = \int_{\mathscr{A}_0} p \, \det(\mathbf{F}) \mathbf{F}^{-T} \cdot \hat{\mathbf{n}}_0 \, dA_0 \tag{14}$$

where the normal is always $\hat{\mathbf{n}}_0 = [0, 0, 1]$ and $\det(\mathbf{F}) = 1$ under the hypothesis of volume constancy. Considering the problem as axisymmetric, we can assume that the components of the pressure along the plane X–Y are self-balanced, so that the resultant $\mathbf{f}^{(p)}$ is directed along the z-axis, i.e. $\mathbf{f}^{(p)} = [0, 0, f_z^{(p)}]$. In actual experiments, the bulge test can deviate from pure axial-symmetry if the material is anisotropic. However, in practice, even if a moderate level of anisotropy is present, such hypothesis is still largely applicable. Applying matrix multiplication to Eq. (14), the only non-zero component $f_z^{(p)}$ becomes:

$$f_z^{(p)} = p \int_{\mathscr{A}_0} F_{33}^{-T} \, dA_0 \tag{15}$$

On the other hand, the force due to the material tension is indicated with $\mathbf{f}^{(t)}$ and depends on the traction force $\mathbf{dt}$. The traction force can be computed in the undeformed configuration exploiting the definition of the Piola–Kirchhoff stress tensor, that maps the stress and the external force in the undeformed configuration. Thus:

$$\mathbf{f}^{(t)} = \int_{\partial \mathscr{A}} \mathbf{dt} = \int_{\partial \mathscr{A}_0} \mathbf{T}^{1PK} \cdot \hat{\mathbf{n}}_0 \, dA_0 \tag{16}$$

where, in this case, the normal is perpendicular to the circumference and is equal to $\hat{\mathbf{n}}_0 = [\cos \alpha, \sin \alpha, 0]$, with α the angle shown in Fig. 2. As discussed before, because of the axial-symmetry, the only non zero component of $\mathbf{f}^{(t)}$ is the one along Z, that is, applying matrix multiplication to Eq. (16):

$$f_z^{(t)} = \int_{\partial \mathscr{A}_0} \left(T_{31}^{1PK} \cos \alpha + T_{32}^{1PK} \sin \alpha \right) \, dA_0 \tag{17}$$

moreover, thanks to the axial symmetry, the term between the parenthesis in Eq. (17) is constant in $\partial \mathscr{A}_0$, therefore the integral can be computed as:

$$f_z^{(t)} = -\kappa \bar{\sigma} (2 \pi R_0 s_0) \tag{18}$$

where $\bar{\sigma}$ is the equivalent stress and κ is a constant defined as:

$$\kappa = -\frac{\left(T_{31}^{1PK} \cos \alpha + T_{32}^{1PK} \sin \alpha \right)}{\bar{\sigma}} \tag{19}$$

This constant can be derived from the measured strain field and the complete steps are detailed in Appendix. To satisfy the equilibrium along Z, the sum of the pressure force (Eq. (15)) and the tension force (Eq. (18)) must be equal to zero, thus:

$$p \int_{\mathscr{A}_0} F_{33}^{-T} \, dA_0 - \kappa \bar{\sigma} (2 \pi R_0 s_0) = 0 \tag{20}$$

and the equivalent stress can be derived as:

$$\bar{\sigma} = \frac{p}{\kappa 2 \pi R_0 s_0} \int_{\mathscr{A}_0} F_{33}^{-T} \, dA_0 \tag{21}$$
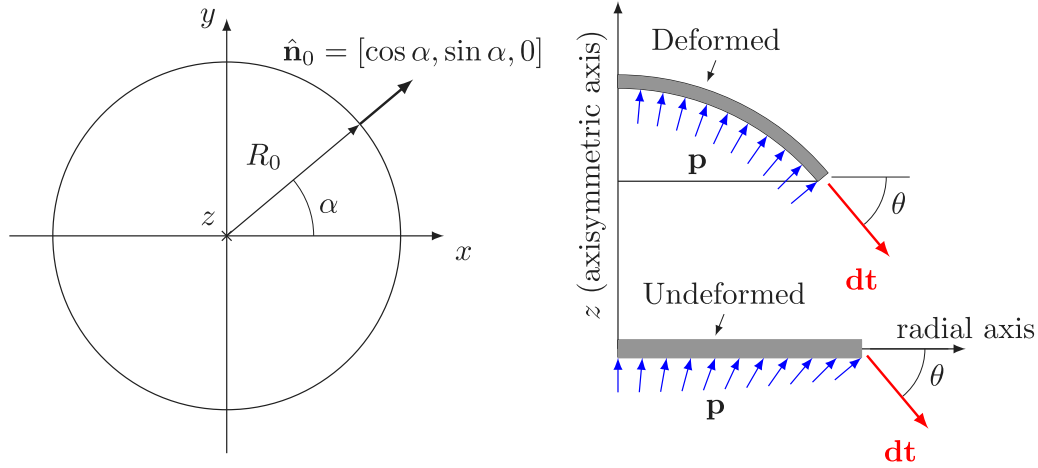
Fig. 2. Circular portion $\mathscr{A}$ of the blank sheet used to retrieve the stress–strain curve; the axial-symmetry and the distribution of the external forces are shown in the right, applied to the undeformed or deformed configuration, respectively.

In actual experiments, the displacement, the strain and the deformation gradient are measured on the specimen surface through image analysis on a discrete number of points. If we have an equispaced grid of points with the same initial area ΔA_0, it follows:

$$\int_{\mathscr{A}_0} F_{33}^{-T}\, dA_0 \approx \Delta A_0 \sum_i^m F_{33\ (i)}^{-T} \approx \frac{\pi R_0^2}{m} \sum_i^m F_{33\ (i)}^{-T} \tag{22}$$

where m are all points inside the circumference with radius R_0. Accordingly, Eq. (21) can be rewritten as:

$$\bar{\sigma} = \frac{pR_0}{\kappa\, 2s_0} \cdot \frac{1}{m} \sum_i^m F_{33\ (i)}^{-T} \tag{23}$$

The corresponding equivalent strain $\bar{\varepsilon}$ can be computed from the strain measurements. In case of isotropic von Mises, neglecting the elastic part, it can be readily obtained as the sum of the equivalent strain increments, i.e. $\bar{\varepsilon} = \sum \Delta\bar{\varepsilon}$, where:

$$\Delta\bar{\varepsilon} = \sqrt{\frac{2}{3}\, \Delta\mathbf{E} : \Delta\mathbf{E}} \tag{24}$$

According to the axial symmetry, the equivalent strain $\bar{\varepsilon}$ is constant in the circumference $\partial\mathscr{A}_0$, therefore, from Eqs. (23) and (24) it comes out directly the stress–strain curve of the material. It is worth noting the used equations do not require the computation of the curvature, since the computation of the first derivative of displacement is sufficient. This should reduce remarkably the noise in experimental applications.

2.2. Principle of virtual work

Another advantage of studying the problem of the bulge test in the reference configuration is that inverse methods developed for 2D applications of sheet metal forming can be readily implemented.

For instance, using the non-linear Virtual Fields Methods (Pierron and Grédiac, 2012), a set of constitutive parameters $\boldsymbol{\xi}$ can be identified by a minimization of a cost function $\psi(\boldsymbol{\xi})$ that represents the balance between the internal and the external virtual work, according to the principle of virtual work (PVW). Using the finite strain theory,[2] the PVW can be written in the reference configuration using the 1st Piola–Kirchhoff tensor, so $\psi(\boldsymbol{\xi})$ becomes:

$$\psi(\boldsymbol{\xi}) = \left| \underbrace{\int_{\mathscr{B}_0} \mathbf{T}^{1PK} : \delta\mathbf{F}^{\bullet}\, dV_0}_{\text{IVW}} - \underbrace{\int_{\partial\mathscr{B}_0} \left(\mathbf{T}^{1PK} \cdot \mathbf{n}_0\right) \cdot \delta\mathbf{v}\, dA_0}_{\text{EVW}} \right| \tag{25}$$

---

[2] In finite strain theory the principle of virtual work is often referred to as the principle of virtual power, however, we prefer to use the term virtual work because it is the most used in the inverse method community.

where the first integral is the internal virtual work (IVW) and the second is the external virtual work (EVW); $\delta\mathbf{v}$ is a kinematically admissible virtual fields and $\delta\mathbf{F}^{\bullet}$ is the corresponding gradient. The parameters $\boldsymbol{\xi}$ are used to compute the stress from the measured strain field using a suitable stress integration algorithm (e.g. radial return, backward Euler, etc.). The virtual fields can be manually defined or automatically chosen using one of the available algorithms, see for instance the papers of Pierron et al. (2016) and Marek et al. (2017, 2019). Given N_v kinematically admissible virtual fields and N_t load steps of the test, the resultant cost function used to identify the parameter $\boldsymbol{\xi}$ becomes:

$$\Psi(\boldsymbol{\xi}) = \frac{1}{N_v N_t} \sum_{i=1}^{N_v} \sum_{j=1}^{N_t} \psi\left(\boldsymbol{\xi}, \delta\mathbf{v}_i, t_j\right) \tag{26}$$

Since Eq. (26) is valid for any virtual field and everything is written in the undeformed configuration, that is a planar sheet, we can always choose a virtual fields so that:

$$\delta\mathbf{v} = \begin{bmatrix} \delta v_x \\ \delta v_y \\ 0 \end{bmatrix} \quad \text{and} \quad \delta\mathbf{F}^{\bullet} = \begin{bmatrix} \delta F_{11}^{\bullet} & F_{12}^{\bullet} & 0 \\ \delta F_{21}^{\bullet} & F_{22}^{\bullet} & 0 \\ 0 & 0 & 0 \end{bmatrix} \tag{27}$$

accordingly, all components in z are equal to zero and the problem reduces to two dimensions. Examples of VFM application will be given in the following sections.

3. Numerical validation

A numerical validation of the proposed method is carried out using a FE model of the HBT. The model is composed by two main parts: the circular die, modeled as a 3D analytic rigid shell, and the blank sheet, which is represented by a deformable shell. Fixed boundary condition is imposed at the external circumference of both parts, while a maximum forming pressure of 80 bar is applied to the blank sheet internal surface. A frictional contact is imposed between the blank sheet and the die, assuming a frictional coefficient of $\mu_s = 0.16$, typical of steel–steel lubricated surfaces. The model is shown in Fig. 3.

Isotropic von Mises plasticity was adopted, using isotropic hardening with the stress–strain curve described with the Swift's law:

$$\bar{\sigma} = K\left(\bar{\varepsilon} + \varepsilon_0\right)^N \tag{28}$$

The model was built using Abaqus/Standard. The sheet metal was simulated using a standard 4-node shell element with reduced integration and hourglass control. The information about geometry, element type and used constitutive parameters are summarized in Table 1.
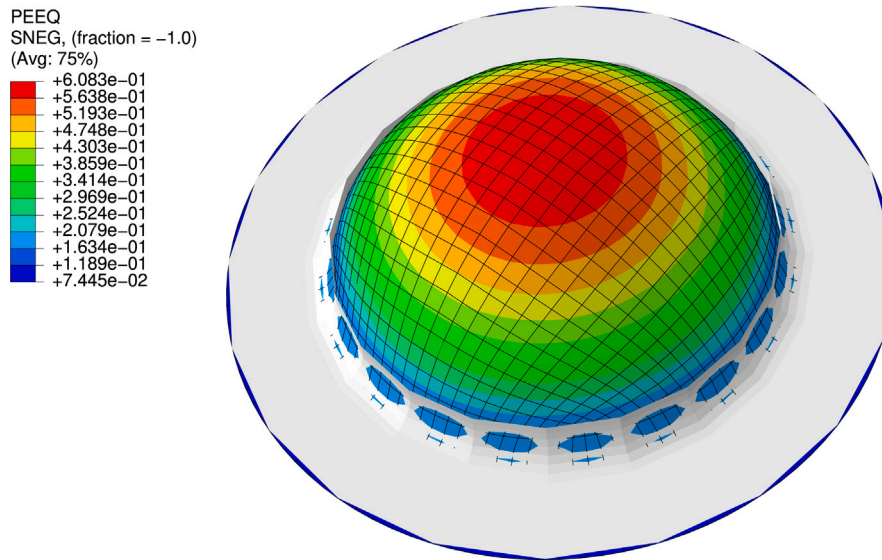
Fig. 3. FE model of the HBT used in the numerical validation, the von Mises equivalent plastic strain is shown.
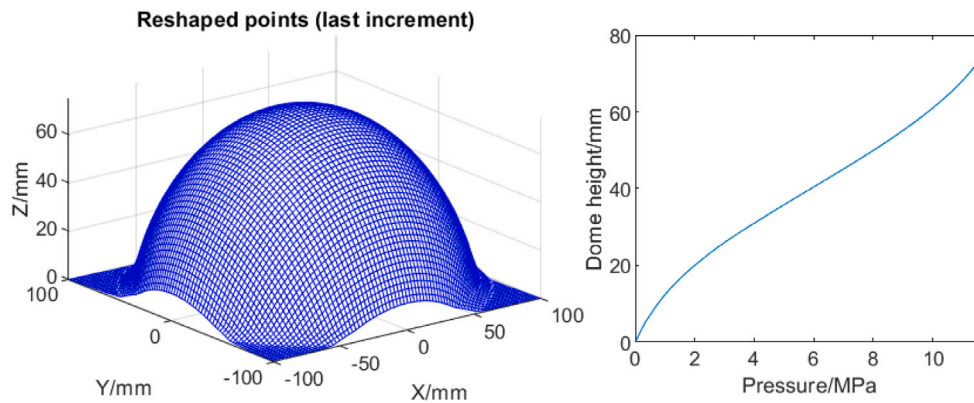

Fig. 4. Points of the bulge test surface at the end of the test and curve of the pressure vs. the maximum height of the dome.

Table 1
Characteristics of the FE model.

Geometry and FE characteristics		Material constitutive parameters	
Blank size	300 mm	Young's modulus	200 GPa
Die diameter	200 mm	Poisson ratio	0.3
Thickness	1.5 mm	K	1000 MPa
Element type	S4R	ε_0	0.02
Number of elements	9716	N	0.5

3.1. Stress–strain curve evaluation

As first step, the nodal displacements from the FE model were reshaped over a regular grid of 2.5×2.5 mm. Fig. 4 shows the reshaped points at the last increment of the simulated test and a plot of the pressure vs. the maximum height of the dome, which can be viewed as typical initial raw data from an experimental bulge test.

From the nodal position, for each point and each step of the test, the deformation gradient $\mathbf{F}$ is computed with Eq. (2) using a standard point-to-point numerical differentiation. From the deformation gradient, the right stretch tensor $\mathbf{U}$ and the true strain $\mathbf{E}$ are obtained as described in Section 2.1. Fig. 5 shows the equivalent plastic strain and the component F_{33}^{-T} of the tensor $\mathbf{F}^{-T}$ (for the last step), plotted in the reference configuration. Given a fixed radius R_0, for each step it is possible to extract a value of equivalent stress from Eq. (23) and the corresponding equivalent strain from Eq. (24). In this case, the true

stress–true strain curve was computed using three different values for the initial radius R_0 (i.e. $R_0 = 40$, 60 and 80 mm) as illustrated in Fig. 5. From the same figure it is also evident that the equivalent plastic strain $\bar{\varepsilon}$ is constant along the different circumferences, because the stress–strain field is axi-symmetric.

The corresponding points of the computed true stress–true strain curve are illustrated in Fig. 6. A good agreement is found with the reference curve, independently from the chosen radius. A rather small underestimation of the stress is observed at the beginning of the curve, this is due to the fact that the elastic part of the strain is neglected in this formulation. Using a smaller radius, the level of equivalent plastic strain is larger (see Fig. 5) because the corresponding strain is larger. With this approach, from the same test, different stress–strain curves can be extracted using different values of the initial radius R_0 and used to calibrate the parameters of an hardening law. The possibility of extracting multiple curves from the same test will reduce the errors due to experimental uncertainties, especially in the initial part of the test, when the curvature is still very low.

3.2. VFM application

The non-linear VFM was applied to identify the hardening behavior of an isotropic material using Eq. (26). As already discussed in Section 2.2, the VFM integrals are computed in the undeformed
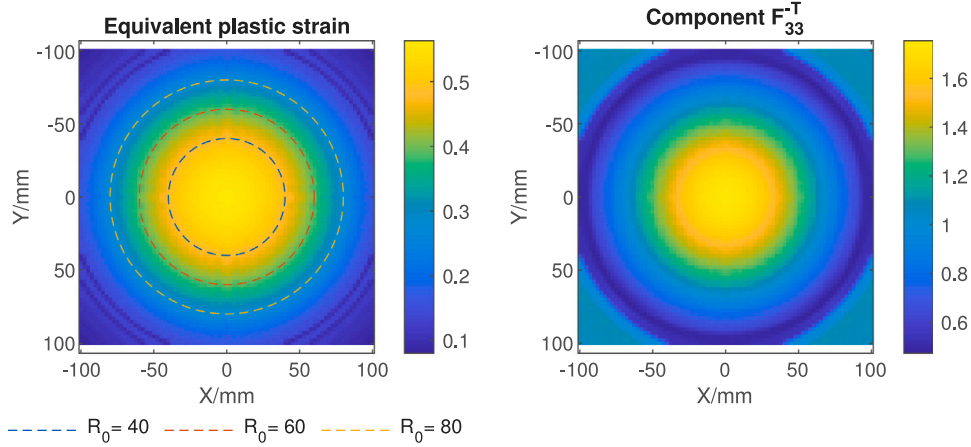
Fig. 5. Equivalent plastic strain and F_{33}^{-T} component computed with the proposed method; in the first plot, the different radii used to compute the stress–strain curve are highlighted.
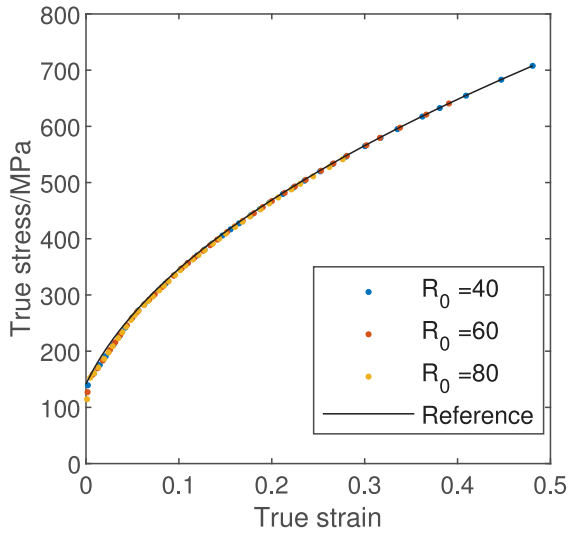

Fig. 6. Comparison of the true stress–true strain points identified with the proposed algorithm and the reference curve.

configuration, using only the in-plane component along X and Y, see Eq. (27). In this case a very simple virtual field was used:

$$\delta\mathbf{v} = \begin{cases} \delta v_x = X \\ \delta v_y = Y \end{cases} \quad \text{with} \quad \delta\mathbf{F}^{\bullet} = \begin{bmatrix} 1 & 0 \\ 0 & 1 \end{bmatrix} \quad (29)$$

The VFM was applied to a circular area $\mathscr{A}_0$ with diameter R_0 (Fig. 2). Under this assumptions, the IVW of Eq. (25) is straightforward:

$$\text{IVW} = \int_{\mathscr{A}_0} \left(T_{11}^{1PK} + T_{22}^{1PK} \right) dv_0 \quad (30)$$

In order to compute the EVW, it is convenient dividing the boundary $\partial\mathscr{A}_0$ into the upper surface, the lower surface and the surface at the circumference border. By definition, the term $\left(\mathbf{T}^{1PK} \cdot \mathbf{n}_0 \, dA_0 \right)$ of Eq. (25) represents the surface forces acting at the boundary $\partial\mathscr{A}_0$. Considering the schematic of Fig. 2, in the upper surface there are no applied forces, thus $\text{EVW}^{\text{upper}} = 0$. In the lower surface, in each point there is the pressure force $(p \, \hat{\mathbf{n}} \, dA)$, which can be rewritten in terms of the reference configuration as $\left(p \det(\mathbf{F}) \mathbf{F}^{-T} \hat{\mathbf{n}}_0 \, dA_0 \right)$, it follows:

$$\text{EVW}^{\text{lower}} = \int_{\partial\mathscr{A}_0^{\text{lower}}} \left(p \det(\mathbf{F}) \mathbf{F}^{-T} \hat{\mathbf{n}}_0 \right) \cdot \delta\mathbf{v} \, dA_0 \quad (31)$$

where $\hat{\mathbf{n}}_0 = \{0, 0, 1\}$, $\delta\mathbf{v}$ is the one of Eq. (29) and $\det(\mathbf{F}) = 1$. Making the matrix multiplication, it follows:

$$\text{EVW}^{\text{lower}} = p \int_{\partial\mathscr{A}_0^{\text{lower}}} \left(F_{13}^{-T} X + F_{23}^{-T} Y \right) dA_0 \quad (32)$$

In the circumference with radius equal to R_0, the virtual field components are equal to $\delta v_x = R_0 \cos\alpha$ and $\delta v_y = R_0 \sin\alpha$, respectively. The virtual field is therefore a vector of length R_0 perpendicular to the circumference in the x–y plane. Assuming the axial-symmetry, the component of the traction force $\mathbf{dt}$ in the X–Y plane is also perpendicular to the circumference and can be computed as $dt_z \cot\theta$, where the angle θ is the one shown in Fig. 2. The EVW in the circumference is thus:

$$\text{EVW}^{\text{circ}} = R_0 \cot\theta \int_{\partial\mathscr{A}_0^{\text{circ}}} dt_z \, dA_0 \quad (33)$$

The last integral of Eq. (33) is exactly the resultant of the vertical forces computed in Eq. (15). Dealing with discrete data, the integrals can be rewritten as sums over the m points internal to the circumference with radius R_0, see Eq. (22). The IVW becomes:

$$\text{IVW} = \frac{\pi R_0^2 s_0}{m} \sum_i^m \left(T_{11 \ (i)}^{1PK} + T_{22 \ (i)}^{1PK} \right) \quad (34)$$

and the EVW:
the EVW is entirely computed from experimental data, i.e. the pressure p and the measured deformation field, used to evaluate $\mathbf{F}^{-T}$. The IVW is computed from the Piola–Kirchhoff stress tensor $\mathbf{T}^{1PK}$ that is a function of the deformation field and the constitutive parameters to be identified, which, in this example, are the parameters of the Swift's law $\boldsymbol{\xi} = \{K, \varepsilon_0, N\}$. The stress is computed from the strain field using the reconstruction algorithm described by Rossi et al. (2020). The cost function to be minimized becomes:

$$\Psi \left(K, \varepsilon_0, N \right) = \frac{1}{N_t} \sum_{i=1}^{N_t} \left| \text{IVW}_i \left(K, \varepsilon_0, N \right) - \text{EVW}_i \right| \quad (35)$$

where N_t is the number of used steps. A constrained gradient descent algorithm, i.e. the matlab function *fmincon*, was used to check the convergence and the accuracy of the VFM algorithm. The results are illustrated in details in Fig. 7 and Table 2. Starting with initial parameters rather different from the reference ones, a fast convergence rate is observed, with the optimal values obtained after 26 iterations. As shown in Fig. 7, the final identified true stress–true strain curve is almost overlapping the reference one. The quality of the identification was assessed as RMS error between theoretical and identified curve. At the final step, an error is still present, because the elastic component of the strain was neglected, however this error is largely acceptable for engineering applications.
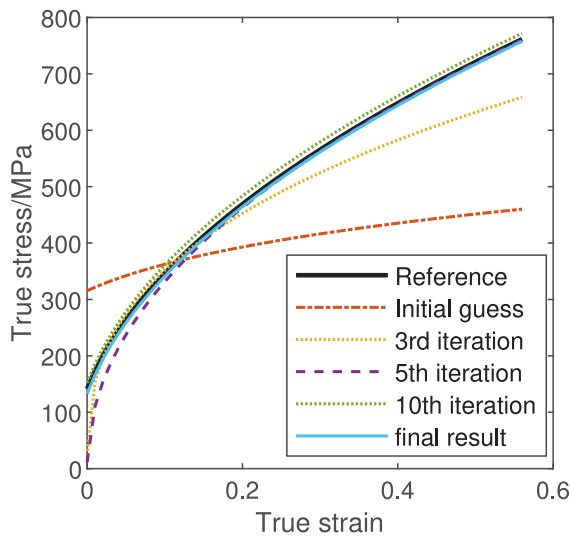
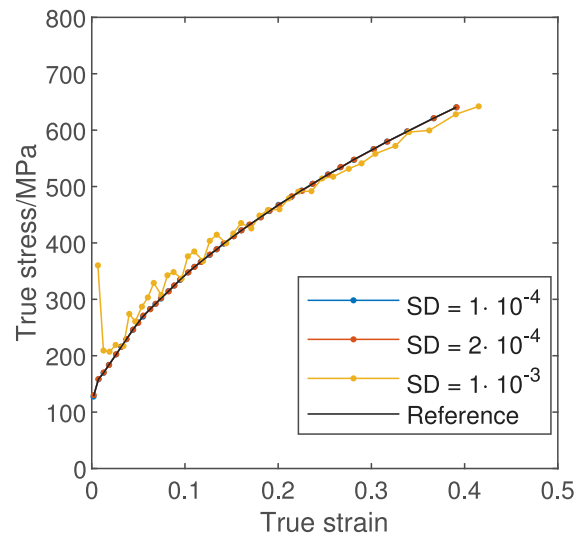**Fig. 7.** Minimization of the constitutive parameter using the non linear VFM.

Fig. 8. True stress–true strain curve identified on noisy strain data.

Table 2
Evolution of the parameters during the minimization algorithm.

Iter.	K	ε_0	N	RMS error (MPa)
0	500	0.1	0.2	173.3
3	813.25	$5.8 \cdot 10^{-5}$	0.364	55.3
5	1005.2	$8.9 \cdot 10^{-5}$	0.482	22.7
10	1003.6	0.0199	0.482	13.2
26	997.7	0.0179	0.5017	4.7
Ref.	1000	0.02	0.5	

Table 3
Evolution of the parameters during the minimization algorithm.

Noise SD	K	ε_0	N	RMS error (MPa)
0	997.7	0.0179	0.5017	4.7
10^{-4}	1000.7	0.0167	0.4986	3.3
$2 \cdot 10^{-4}$	1002.0	0.0178	0.5013	2.8
10^{-3}	979.8	0.0165	0.4862	6.7
Ref.	1000	0.02	0.5	

3.3. Effect of noise

In order to evaluate the sensitivity of the proposed method to experimental uncertainties, a preliminary study was conducted adding a Gaussian noise to the strain maps obtained from the numerical analysis. It is generally accepted that, for a typical DIC measurement, the standard deviation (SD) of the noise, in term of microstrain, is below 100 μm/m, see for instance the work of Badaloni et al. (2015). In this case, three levels of noise were considered, with SD equal to 100, 200 and 1000 μm/m. The latter represents an extremely severe noise level.

Fig. 8 illustrates the identification of the true stress–true strain curve performed with noisy data using the algorithm described in Section 2.1. The effect of noise is visible only if the severe and unrealistic level of noise is added. Table 3 shows the parameters identified with the VFM on noisy data. Again the identification is almost unaffected by the noise, even in the high noise level case.

This analysis demonstrates that the proposed algorithm is robust and almost insensitive to random noise. However, to keep into account the whole experimental uncertainties (including effect of speckle pattern, spatial resolution of the used camera, light variations, effect of calibration, etc.) it is necessary to simulate the whole measurement chain using a virtual test and a simulator as the one developed by Balcaen et al. (2017) for stereo-DIC. In this paper, an actual test was

used to illustrate the suitability of the proposed approach to real cases, however, in the future, further analyses will be conducted to better quantify the accuracy.

4. Experiments

4.1. Experimental set-up

In this section, the proposed identification approach was used to retrieve the hardening curve from the bulge test on a bake-hardened steel, namely the BH340 from POSCO. The hydraulic bulge test was performed on a 300×300 mm^2 square specimen obtained from a blank sheet of BH340 steel with 0.7 mm of thickness through wire EDM cutting. The test was carried out in quasi-static conditions by employing an Erichsen® BULGE-FLC 161 hydraulic machine, designed for forming bulges with 200 mm of diameter with a max drawing force of 1000 kN. The full-field deformation of the specimen was measured by using the stereo-DIC technique, assisted by two 2448×2048 pixel^2 Point Grey Grasshopper GRAS-50S5M-C cameras, as shown in Fig. 9. Here, the image analysis was achieved with the commercial software MatchID® (www.matchid.eu, version 2018.2.2), adopting the correlation settings listed in Table 4.

The same experiment was already used in Lattanzi et al. (2020) for the calibration of an advanced anisotropic plasticity model: the Yld2000-2D. We decided to use this test to validate the presented procedure because the material approximates the isotropic behavior in a zone of the stress space close to the equi-biaxial state. This is testified by the r-value in the biaxial state ($r_{\text{biax}} = 0.98$), which represents the slope of the yield surface at balanced biaxial stress state, i.e. $r_{\text{biax}} = \dot{\varepsilon}_{xx}/\dot{\varepsilon}_{xx}$. The complete set of r-values and the ratios of the uniaxial stress σ_u to the biaxial stress σ_b measured in different directions are listed in Table 5.

4.2. Data elaboration

As first step, the displacement field obtained with stereo-DIC was reshaped over a regular grid with a constant spacing of 2.5×2.5 mm, using a scattered data interpolation function. Each point of the regularized mesh is thus computed using several experimental points, as illustrated in Fig. 10. Moreover, 41 load steps were sampled from the initial 698 ones. The reduced number of steps avoid the experimental uncertainties tied to pressure measurement, preserving at the same time the load history, as illustrated in the second plot of Fig. 10.

Table 4
DIC analysis settings for the hydraulic bulge test.

Camera	Point Grey Grasshopper GRAS-50S5M-C
Image resolution	2448 × 2048, 14-bit
Field of view	315.8 × 264.25 mm
Pixel to mm conversion	1 pixel = 0.12903 mm
Stereo-angle	12.4°
Stand-off distance	650 mm
Patterning technique	Matt white spray paint base coat with black speckles
Pattern feature size (approx.)	4.2 pixel/0.54 mm
DIC technique	Stereo correlation
DIC software	MatchID, version 2018.2.2
Image filtering	Gaussian, 5 × 5 pixel kernel
Subset size	43 pixels/5.29 mm
Step size	7 pixels/0.90 mm
Subset shape function	Affine
Matching criterion	Zero-normalized sum of square differences (ZNSSD)
Interpolant	Bi-cubic spline
Stereo transformation	Affine
Strain formulation	Hencky logarithmic
Spatial smoothing	Local polynomial regression Q8, 15 × 15 window
Temporal smoothing	N/A
Virtual strain gauge size	139 pixels/17.93 mm
Displacement noise floor	0.008 pixels/0.28 μm (in plane); 2.0 μm (out-of-plane)
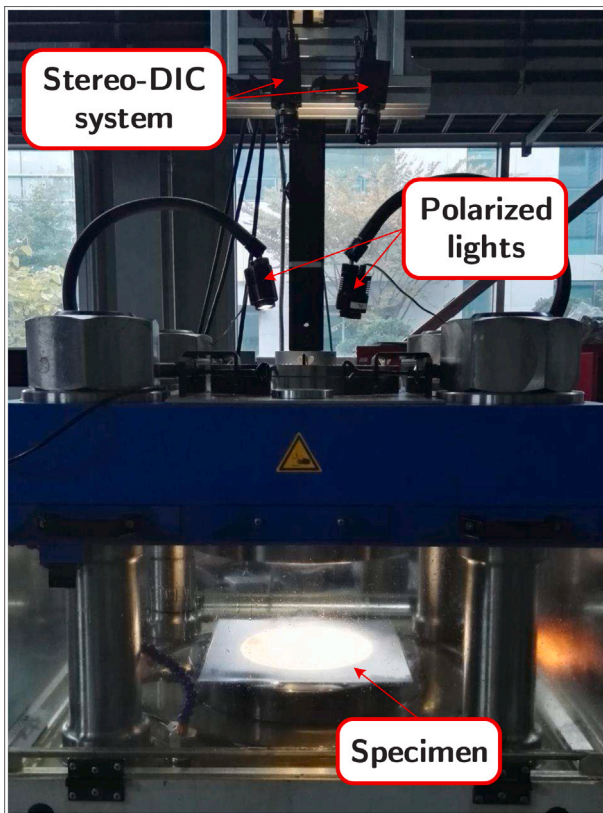
Fig. 9. Experimental set-up adopted for the hydraulic bulge test, the illumination and the used stereo-DIC system are illustrated.

Table 5
Experimental data for the material BH340 used in the experiments (Lattanzi et al., 2020).

Dir.	0°	15°	30°	45°	60°	75°	90°	Biax.
r-value	0.92	0.92	0.95	0.96	0.96	0.93	0.92	0.98
σ_u/σ_b	1.52	1.30	1.00	0.89	1.06	1.48	1.67	1

It is worth noting the described data regularization is the only smoothing applied to the experimental data. For each load step, the

Table 6
Parameters of two hardening laws fitted over the experimental data from the Bulge test.

Swift's model			
K	ε_0	N	RSM error
702.56 MPa	0.0020	0.2470	10.8 MPa

Modified Voce's model				
σ_Y	A	B	H	RSM error
173.11 MPa	238.51 MPa	18.6	354.54 MPa	5.5 MPa

deformation gradient **F** is obtained from Eq. (2) using a point-to-point numerical differentiation. From a computational point of view, the use of a regular grid considerably simplifies the data elaboration, which can be efficiently performed using matrix operations.

An example of computed strain map is given in Fig. 11 where the von Mises equivalent strain for the last step of the test is depicted. In the same graph, the radii of the areas used to compute the true stress–true strain curve are also plotted. As explained before, only the points inside the circle are used for the curve identification.

5. Results and discussion

The plot of Fig. 12 illustrates the curves identified using three different radii, similar results are obtained in all cases. With respect to uniaxial tensile tests, the HBT allows to identify the hardening curve up to large values of the true strain, because the necking in a biaxial state of stress arises later on. In this case, the curve was identified up to 0.55 m/m. With the proposed identification method, the curve was accurately identified also at the early stage of the test when the true strain is below 0.1. This zone is particularly critical in the HBT because of the low deformation of the sheet, especially if the true stress is computed from the curvature, as commonly established from the test standards.

The experimental points can be used to identify the parameters of a hardening law. Indeed, FE analysis of forming sometimes requires the use of analytical constitutive laws, such as Voce or Swift curve, and the HTB can be applied to get the best possible response that fits to experimental data. Here the Swift's law:

$$\bar{\sigma} = K \left(\bar{\varepsilon} + \varepsilon_0 \right)^N \tag{36}$$

where K, ε_0 and N are the constitutive parameters, and a modified Voce's law:

$$\bar{\sigma} = \sigma_Y + A \left(1 - e^{-B\bar{\varepsilon}} \right) + H\bar{\varepsilon} \tag{37}$$

where σ_Y, A, B and H are the constitutive parameters, were employed. Both models shows a good agreement with the experimental data, see Fig. 12. The identified parameters as well as the RMS error are listed in Table 6, a slightly better result is obtained using the modified Voce's model.

To verify if the test is axi-symmetric, Fig. 13 shows the evolution of the equivalent plastic strain measured in a circular path with initial radius $R_0 = 30$ mm. Especially in the last steps of the test, the path plots are not perfectly constant, although the deviation is still reasonably small. This can be due to experimental uncertainties, misalignment, anisotropy material inhomogeneities, etc. However, practically, the equivalent strain for each step is computed as the mean of the values obtained in the circular path, thus such deviation has a minimal impact in the determination of the hardening curve.

As final study, the same VFM approach described in Section 3 was applied to the experimental data to identify the parameters of a Swift's hardening law. The circular area used to compute the VFM has an initial radius $R_0 = 30$ mm. The identified parameters were $K = 689.03$, $\varepsilon_0 = 0.0015$ and $N = 0.2353$. Those parameters are slightly different from the ones estimated with the first method and listed in Table 6, however,
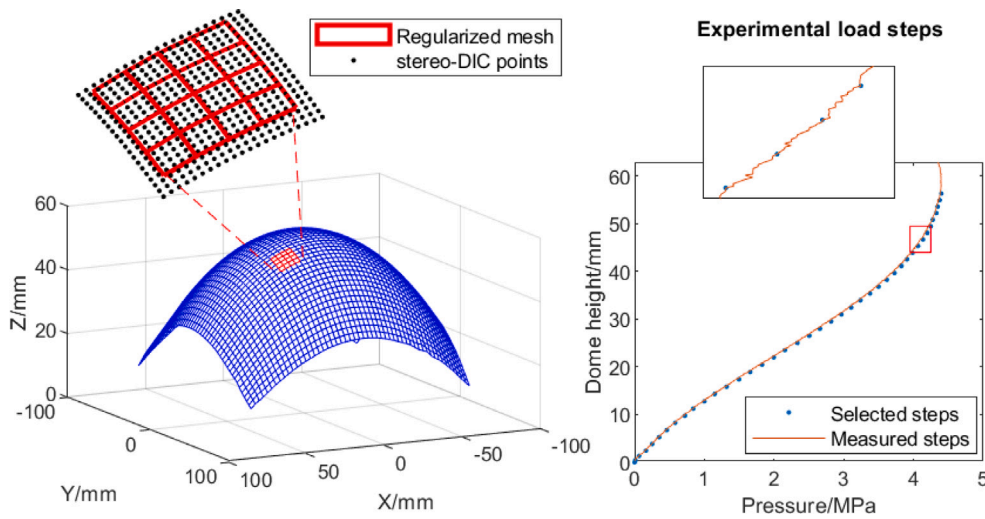
Fig. 10. On the left: experimental points obtained after the reshaping operation from the stereo-DIC data; on the right, pressure vs. dome height curve and steps selected for the identification procedure.
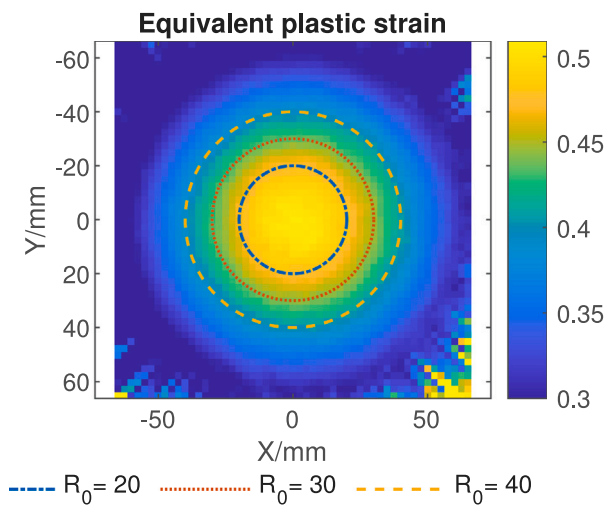

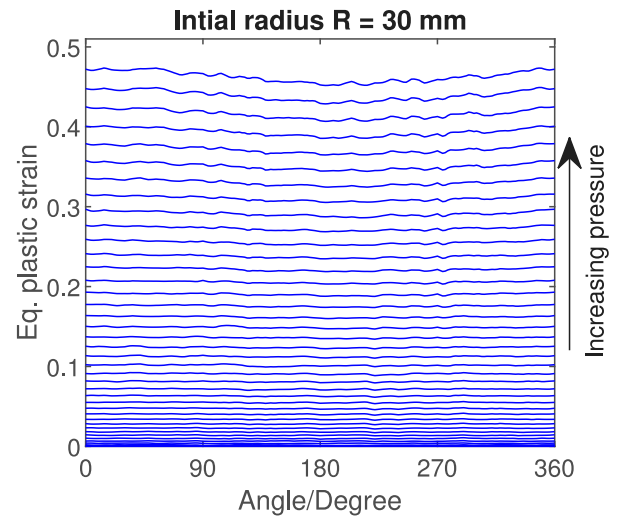**Fig. 11.** Example of equivalent strain map obtained from the experiments.

Fig. 13. Evolution of the equivalent plastic strain during the test in the circle with initial radius $R_0 = 30$.
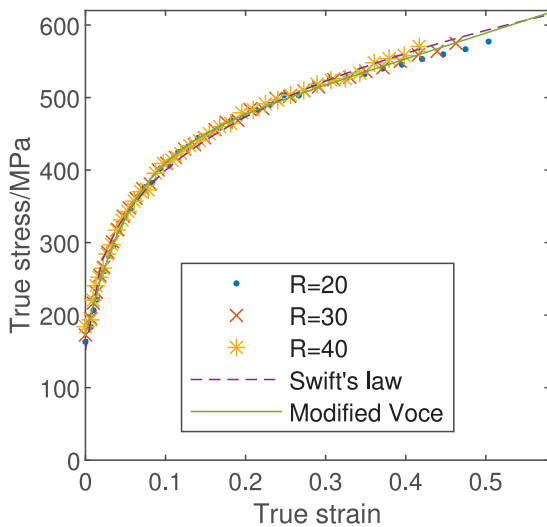

Fig. 12. Points of the true stress–true strain curve identified using the proposed algorithm for three different radii and curve fitting obtained with two popular hardening models, i.e. Swift's law and modified Voce.

the corresponding hardening curves are rather similar, as illustrated in Fig. 14. As a term of comparison, in the same graph, the curve identified using the ISO standard is also plotted. A good agreement is obtained with the different approaches, demonstrating the reliability of the proposed method. The small deviation observed between the identified curves and the ISO standard can be due to the different post-processing method, based on the curvature, and to the choice of the Swift's law as hardening model. For instance, Chen et al. (2018) showed that, for certain materials, Swift and Voce models are not able to reproduce the actual curve extracted from a bulge test. However, in this case, the mismatch is rather low and the Swift assumption is reasonably accurate for the validation purpose of this work.

Finally, it must be underlined that the identified curve represents the stress–strain relation in the biaxial state, that will be different from the one obtained in a uniaxial test because the material is anisotropic. Anisotropy can be included in the VFM approach employing a suitable anisotropic criterion to compute the stress from the strain. Moreover the bulge test can be used in conjunction with other tests (e.g notched specimens, uniaxial tests, elliptical bulge tests, etc.) to improve the quality of the identification. In fact, often the VFM algorithm is run over multiple experiments at the same time in order to identify the
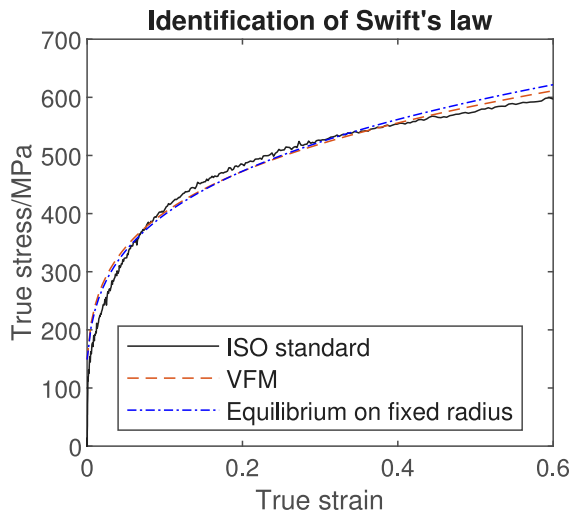
Identification of Swift's law

Fig. 14. Comparison of the hardening curve identified using the VFM and the equilibrium method, in both cases the Swift's law was used as hardening model. The corresponding curve obtained with the ISO standard is also reported.

constitutive parameters of advanced plasticity models (Lattanzi et al., 2020).

The application of the presented method to anisotropic materials, however, is beyond the scope of this paper and will be addressed in future works.

6. Conclusion

In this paper, a novel method to identify the plastic behavior of materials using the HBT and full-field measurement is presented. With respect to the conventional method, this approach has the advantage of using the whole full-field measurement information and avoid the computation of the curvature, which requires a double derivative of experimental data. A numerical validation is performed using a FE model of the test, then the procedure was applied to a real experiment to extract the hardening behavior in terms of true stress–true strain curve. The approach was also used to demonstrate the possibility of applying the VFM, developed for plane stress condition, to HBT. The main outcomes of this paper are:

- a consistent framework to elaborate full-field displacement data of a HBT obtained from stereo-DIC is presented. For each point, the complete deformation tensor $\mathbf{F}$ is computed using the volume constancy hypothesis, then the strain and stress fields are mapped onto the initial undeformed configuration using the finite deformation theory.
- The implementation of the method is computationally effective and suitable for large experimental data. In fact everything is obtained using simple operations, like point-to-point differentiation, matrix multiplication or sum, that can be easily vectorized.
- The procedure is less sensitive to noise because it is not necessary to evaluate the curvature but only the first derivative of the displacement field, for instance, in the presented application it was not necessary to apply any smoothing function to have reliable results.
- The proposed approach allows to include effectively the bulge test in inverse identification schemes developed for 2D plane stress applications, since everything is mapped in the initial configuration that is a flat sheet metal.
- An algorithm to retrieve directly the true stress–true strain curve is derived exploiting the equilibrium equation on a fixed initial radius R_0, the algorithm is summarized by Eq. (23). In this way,

from a single test it is possible to extract different curves at different radii, reducing the impact of experimental uncertainties and increasing the amount of information achievable from a single test.
- The VFM was applied to HBT in order to identify the hardening behavior of the material using a Swift's law. Reliable results were obtained using both numerical and experimental data. It is worth noting that the VFM approach is the same already used for 2D plane stress applications.
- In this paper, the identification framework was validated using isotropic plasticity, in order to precisely assess the accuracy of the method and the impact of the approximations, however, it is necessary to perform simulated experiments that include the effect of experimental uncertainties and the anisotropy.

The results illustrated in this paper foster the use of the HBT in inverse methods. Although a standard circular bulge test was investigated in this paper, in the future, different shape of the hole (elliptical, squared, etc.) could be used to increase the heterogeneity of the stress/strain field and enrich the information about the material behavior achievable from a single test. It should be also noted that the proposed approach is specifically targeted for inverse methods, if the bulge test is used to retrieve the stress–strain curve at the bulge apex, the conventional methods based on the curvature remains a valid alternative. A quantitative comparison of the accuracy of the two characterization approaches is beyond the scope of this paper and may be addressed in future works.

Declaration of competing interest

The authors declare that they have no known competing financial interests or personal relationships that could have appeared to influence the work reported in this paper.

Appendix

In order to compute the equivalent stress with Eq. (23), it is necessary to evaluate the constant κ defined by Eq. (19):

$$\kappa = -\frac{\left(T_{31}^{1PK}\cos\alpha + T_{32}^{1PK}\sin\alpha\right)}{\bar{\sigma}} \quad (19)$$

where only the angle α is known. Following the definition of the 1st Piola–Kirchhoff stress given in Eq. (12), in order to compute κ we need to retrieve the components of $\mathbf{T}^{1PK}$ normalized with respect to $\bar{\sigma}$, that is:

$$\frac{\mathbf{T}^{1PK}}{\bar{\sigma}} = \det(\mathbf{F})\,\hat{\boldsymbol{\sigma}}\,\mathbf{F}^{-T} \quad \text{with} \quad \hat{\boldsymbol{\sigma}} = \boldsymbol{\sigma}/\bar{\sigma} \quad (38)$$

Since $\det(\mathbf{F}) = 1$ and $\mathbf{F}^{-T}$ is computed from the measured displacement field, the only unknown is the normalized Cauchy stress $\hat{\boldsymbol{\sigma}}$, that can be obtained from the plastic flow rule. In the material reference system, the plastic flow is directed as the increment $\Delta\mathbf{E}$ of the logarithmic strain defined by Eq. (11). Using the associative flow rule with von Mises,[3] the direction of the stress $\hat{\mathbf{n}}^\sigma$ in the plane X–Y

---

[3] The procedure can be easily extended to other flow rules and yielding models, see Rossi et al. (2020) for details.
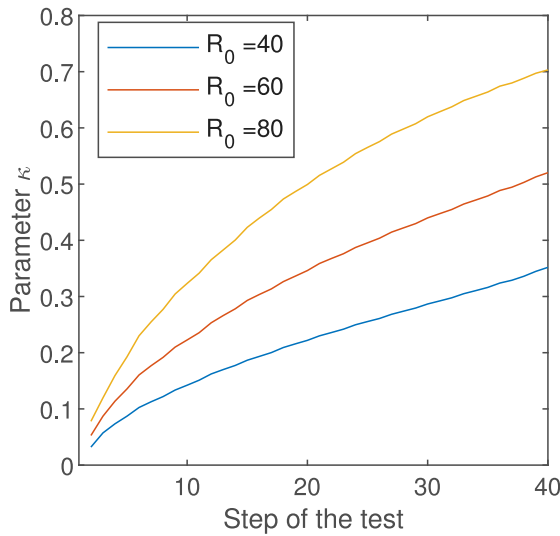
Fig. 15. *kappa* parameter.

can be then retrieved as:

$$
\begin{bmatrix} \hat{n}_X^\sigma \\ \hat{n}_Y^\sigma \\ \hat{n}_{XY}^\sigma \end{bmatrix} = \frac{\begin{bmatrix} 1 & 0.5 & 0 \\ 0.5 & 1 & 0 \\ 0 & 0 & 0.5 \end{bmatrix} \cdot \begin{bmatrix} \Delta E_{11} \\ \Delta E_{22} \\ \Delta E_{12} \end{bmatrix}}{\left\| \begin{bmatrix} 1 & 0.5 & 0 \\ 0.5 & 1 & 0 \\ 0 & 0 & 0.5 \end{bmatrix} \cdot \begin{bmatrix} \Delta E_{11} \\ \Delta E_{22} \\ \Delta E_{12} \end{bmatrix} \right\|}
\tag{39}
$$

then, in order to obtain the normalized stress $\hat{\sigma}$, the stress directions obtained in the material reference plane must be rotated in the deformed configuration and normalized according to the equivalent stress function, i.e.:

$$
\hat{\sigma} = \frac{[\mathbf{R}]^T \cdot \begin{bmatrix} \hat{n}_X^\sigma & \hat{n}_{XY}^\sigma & 0 \\ \hat{n}_{XY}^\sigma & \hat{n}_Y^\sigma & 0 \\ 0 & 0 & 0 \end{bmatrix} \cdot [\mathbf{R}]}{\sqrt{\hat{n}_X^{\sigma\,2} + \hat{n}_Y^{\sigma\,2} - \hat{n}_X^\sigma \hat{n}_Y^\sigma + 3\,\hat{n}_{XY}^{\sigma\,2}}}
\tag{40}
$$

where $\mathbf{R}$ is the rotation matrix computed in Section 2. Applying in sequence Eqs. (39), (40), (38) and (19) the parameter κ is obtained for each step of the test and for a given radius R_0. The operations are all matrix multiplications or sums that can be easily vectorized and computed without significant computational cost, even if a large amount of full-field data are available.

As an example, Fig. 15 illustrates the evolution of the parameter κ during the test for the three different radii used in the numerical validation of Section 3.

References

Avril, S., Bonnet, M., Bretelle, A.-S., Grédiac, M., Hild, F., Ienny, P., Latourte, F., Lemosse, D., Pagano, S., Pagnacco, E., et al., 2008. Overview of identification methods of mechanical parameters based on full-field measurements. Exp. Mech. 48 (4), 381–402.

Badaloni, M., Rossi, M., Chiappini, G., Lava, P., Debruyne, D., 2015. Impact of experimental uncertainties on the identification of mechanical material properties using DIC. Exp. Mech. 55 (8), 1411–1426.

Balcaen, R., Wittevrongel, L., Reu, P.L., Lava, P., Debruyne, D., 2017. Stereo-DIC calibration and speckle image generator based on FE formulations. Exp. Mech. 57 (5), 703–718.

Barlat, F., Aretz, H., Yoon, J.W., Karabin, M., Brem, J., Dick, R., 2005. Linear transfomation-based anisotropic yield functions. Int. J. Plast. 21 (5), 1009–1039.

Barnwal, V.K., Lee, S.-Y., Choi, J., Kim, J.-H., Barlat, F., 2021. On the fracture characteristics of advanced high strength steels during hydraulic bulge test. Int. J. Mech. Sci. 190, 106032.

Bunge, H., Pöhlandt, K., Tekkaya, A., 2000. Formability of Metallic Materials: Plastic Anisotropy, Formability Testing, Forming Limits. Springer Science & Business Media.

Chen, K., 2020. A general and unified theory of the kinematic relationships in bulge tests. J. Mech. Phys. Solids 143, 104086.

Chen, K., Scales, M., Kyriakides, S., 2018. Material hardening of a high ductility aluminum alloy from a bulge test. Int. J. Mech. Sci. 138, 476–488.

Chen, K., Scales, M., Kyriakides, S., Corona, E., 2016. Effects of anisotropy on material hardening and burst in the bulge test. Int. J. Solids Struct. 82, 70–84.

Cooreman, S., Lecompte, D., Sol, H., Vantomme, J., Debruyne, D., 2008. Identification of mechanical material behavior through inverse modeling and DIC. Exp. Mech. 48 (4), 421–433.

Coppieters, S., Cooreman, S., Sol, H., Van Houtte, P., Debruyne, D., 2011. Identification of the post-necking hardening behaviour of sheet metal by comparison of the internal and external work in the necking zone. J. Mater. Process. Technol. 211 (3), 545–552.

Fu, J., Barlat, F., Kim, J.-H., Pierron, F., 2017. Application of the virtual fields method to the identification of the homogeneous anisotropic hardening parameters for advanced high strength steels. Int. J. Plast. 93, 229–250.

Grédiac, M., Hild, F., 2013. Full-Field Measurements and Identification in Solid Mechanics. Wiley Online Library.

Gutscher, G., Wu, H.-C., Ngaile, G., Altan, T., 2004. Determination of flow stress for sheet metal forming using the viscous pressure bulge (vpb) test. J. Mater. Process. Technol. 146 (1), 1–7.

Hérault, D., Thuillier, S., Lee, S.-Y., Manach, P.-Y., Barlat, F., 2021. Calibration of a strain path change model for a dual phase steel. Int. J. Mech. Sci. 194, 106217.

Hill, R., 1950. C. a theory of the plastic bulging of a metal diaphragm by lateral pressure. Lond. Edinb. Dublin Philos. Mag. J. Sci. 41 (322), 1133–1142.

Kajberg, J., Lindkvist, G., 2004. Characterisation of materials subjected to large strains by inverse modelling based on in-plane displacement fields. Int. J. Solids Struct. 41 (13), 3439–3459.

Kim, J.-H., Barlat, F., Pierron, F., Lee, M.-G., 2014. Determination of anisotropic plastic constitutive parameters using the virtual fields method. Exp. Mech. 54 (7), 1189–1204.

Koç, M., Billur, E., Cora, Ö.N., 2011. An experimental study on the comparative assessment of hydraulic bulge test analysis methods. Mater. Des. 32 (1), 272–281.

Kuwabara, T., Sugawara, F., 2013. Multiaxial tube expansion test method for measurement of sheet metal deformation behavior under biaxial tension for a large strain range. Int. J. Plast. 45, 103–118.

Lattanzi, A., Barlat, F., Pierron, F., Marek, A., Rossi, M., 2020. Inverse identification strategies for the characterization of transformation-based anisotropic plasticity models with the non-linear VFM. Int. J. Mech. Sci. 173, 105422.

Lee, J.-Y., Xu, L., Barlat, F., Wagoner, R., Lee, M.-G., 2013. Balanced biaxial testing of advanced high strength steels in warm conditions. Exp. Mech. 53 (9), 1681–1692.

Marek, A., Davis, F.M., Pierron, F., 2017. Sensitivity-based virtual fields for the non-linear virtual fields method. Comput. Mech. 60 (3), 409–431.

Marek, A., Davis, F.M., Rossi, M., Pierron, F., 2019. Extension of the sensitivity-based virtual fields to large deformation anisotropic plasticity. Int. J. Mater. Form. 12 (3), 457–476.

Meuwissen, M., Oomens, C., Baaijens, F., Petterson, R., Janssen, J., 1998. Determination of the elasto-plastic properties of aluminium using a mixed numerical–experimental method. J. Mater. Process. Technol. 75 (1–3), 204–211.

Mulder, J., Vegter, H., Aretz, H., Keller, S., van den Boogaard, A.H., 2015. Accurate determination of flow curves using the bulge test with optical measuring systems. J. Mater. Process. Technol. 226, 169–187.

Pierron, F., Avril, S., Tran, V.T., 2016. Extension of the virtual fields method to elasto-plastic material identification with cyclic loads and kinematic hardening. Int. J. Solids Struct. 47 (22–23), 2993–3010.

Pierron, F., Grédiac, M., 2012. The Virtual Fields Method: Extracting Constitutive Mechanical Parameters from Full-Field Deformation Measurements. Springer Science & Business Media.

Pradeau, A., Thuillier, S., Yoon, J.W., 2016. Prediction of failure in bending of an aluminium sheet alloy. Int. J. Mech. Sci. 119, 23–35.

Prates, P., Pereira, A., Sakharova, N., Oliveira, M., Fernandes, J., 2016. Inverse Strategies for Identifying the Parameters of Constitutive Laws of Metal Sheets. Adv. Mater. Sci. Eng. 4152963.

Rossi, M., Cortese, L., Genovese, K., Lattanzi, A., Nalli, F., Pierron, F., 2018a. Evaluation of volume deformation from surface dic measurement. Exp. Mech. 58 (7), 1181–1194.

Rossi, M., Lattanzi, A., Barlat, F., 2018b. A general linear method to evaluate the hardening behaviour of metals at large strain with full-field measurements. Strain 54 (3), e12265.

Rossi, M., Lattanzi, A., Cortese, L., Amodio, D., 2020. An approximated computational method for fast stress reconstruction in large strain plasticity. Internat. J. Numer. Methods Engrg. 121 (14), 3048–3065.

Rossi, M., Pierron, F., 2012. Identification of plastic constitutive parameters at large deformations from three dimensional displacement fields. Comput. Mech. 49 (1), 53–71.

Rossi, M., Pierron, F., Štamborská, M., 2016. Application of the virtual fields method to large strain anisotropic plasticity. Int. J. Solids Struct. 97 (2016), 322–335.

Sutton, M.A., Orteu, J.J., Schreier, H., 2009. Image Correlation for Shape, Motion and Deformation Measurements: Basic Concepts, Theory and Applications. Springer Science & Business Media.

Williams, B.W., Boyle, K.P., 2016. Characterization of anisotropic yield surfaces for titanium sheet using hydrostatic bulging with elliptical dies. Int. J. Mech. Sci. 114, 315–329.

Young, R., Bird, J., Duncan, J., 1981. An automated hydraulic bulge tester. J. Appl. Metalwork. 2 (1), 11–18.

Zang, S., Thuillier, S., Le Port, A., Manach, P.-Y., 2011. Prediction of anisotropy and hardening for metallic sheets in tension, simple shear and biaxial tension. Int. J. Mech. Sci. 53 (5), 338–347.

Zhang, L., Thakku, S.G., Beotra, M.R., Baskaran, M., Aung, T., Goh, J.C., Strouthidis, N.G., Girard, M.J., 2017. Verification of a virtual fields method to extract the mechanical properties of human optic nerve head tissues in vivo. Biomech. Model. Mech. 16 (3), 871–887.